

Communication

# Full-Color and Anti-Counterfeit Printings with All-Dielectric Chiral Metasurfaces

Longjie Li <sup>1,2,3</sup>, He Li <sup>1,2,3</sup>, Huakui Hu <sup>1,2,3</sup>, Xiao Shang <sup>1,2,3</sup>, Huiwen Xue <sup>1,2,3</sup>, Jinyu Hu <sup>1,2,3</sup>, Cheng Lu <sup>1,2</sup>, Shengjie Zhao <sup>1,2</sup>, Jiebin Niu <sup>1,2,\*</sup> and Lina Shi <sup>1,2,\*</sup>

<sup>1</sup> State Key Lab of Fabrication Technologies for Integrated Circuits, Institute of Microelectronics of the Chinese Academy of Sciences, No. 3 West Road, Beitucheng, Beijing 100029, China

<sup>2</sup> Laboratory of Microelectronic Devices and Integrated Technology, Institute of Microelectronics of the Chinese Academy of Sciences, No. 3 West Road, Beitucheng, Beijing 100029, China

<sup>3</sup> University of Chinese Academy of Sciences, 19 Yuquan Road, Shijingshan District, Beijing 100049, China

\* Correspondence: niujiebin@ime.ac.cn (J.N.); shilina@ime.ac.cn (L.S.)

**Simple Summary:** Structural color is a vibrant color produced by optical effects such as interference, diffraction, or scattering of incident light interacting with the nanostructure, which has the advantages of environmental protection, high saturation, and high resolution. High saturation and dynamic tunability are the current research hotspots for structural color. We achieve full-color wide gamut structural colors and anti-counterfeit functions by an all-dielectric chiral metasurface consisting of half-gammadion-shaped resonators embedded in PMMA and a top TiO<sub>2</sub> layer on quartz coated with an ITO layer. This research has significant implications in micro-display, nano-printing, anti-counterfeiting, and information encryption.

**Abstract:** Structural color is anticipated to replace pigmented or chemical color due to its superior saturation, resolution, environmental friendliness, and longevity. We achieve a full-color gamut of structural colors and anti-counterfeit functions by an all-dielectric chiral metasurface consisting of half-gammadion-shaped resonators embedded in PMMA and a top TiO<sub>2</sub> layer on quartz coated with an ITO layer. The prominent resonance peaks of this embedded chiral metasurface under the cross-polarization condition, which are provided by the polarization conversion features of the chiral structure, lead to extremely saturated structural colors. The color phase mainly depends on the structure's period, opening up a full-color range well beyond sRGB. Especially, we demonstrate a star with hidden information of the letter "A" and the Chinese word "李龙杰" by taking advantage of the difference in the color phase change under different polarization conditions to decode the information, thus realizing the anti-counterfeiting function. Our proposed embedded chiral metasurface provides dual-function structural colors and is highly promising for micro-display, nanoprinting, anti-counterfeiting, data storage, and information encryption.

**Keywords:** structural color; metasurface; chiral; anti-counterfeit



**Citation:** Li, L.; Li, H.; Hu, H.; Shang, X.; Xue, H.; Hu, J.; Lu, C.; Zhao, S.; Niu, J.; Shi, L. Full-Color and Anti-Counterfeit Printings with All-Dielectric Chiral Metasurfaces. *Photonics* **2023**, *10*, 401. <https://doi.org/10.3390/photonics10040401>

Received: 6 March 2023

Revised: 21 March 2023

Accepted: 24 March 2023

Published: 3 April 2023



**Copyright:** © 2023 by the authors. Licensee MDPI, Basel, Switzerland. This article is an open access article distributed under the terms and conditions of the Creative Commons Attribution (CC BY) license (<https://creativecommons.org/licenses/by/4.0/>).

## 1. Introduction

When compared to pigments and bioluminescence, structural color is a gift from nature that may be used to create a colorful and sustainable world due to the advantages of non-polluting, high resolution, high saturation, and durability, which are generated through the interference and scattering of light from the nanostructure [1]. An improvement in the utilization of plasmonic and all-dielectric metasurfaces to create artificial structural colors has been attributed to recent developments in nanofabrication techniques [2]. Optical responses for plasmonic structural colors represented by Au [3–5], Ag [6–10], and Al [11–15] are mainly driven by plasmonic resonances based on a variety of metallic nanostructures, but this is constrained by the inherent ohmic loss of the metal,

leading to a subpar structural color performance. Yet the electric and magnetic dipole resonances generated from high-index dielectric materials simultaneously adapt to govern the spectrum and achieve high-saturation colors [16], as shown by the dielectric structural colors represented by Si [17–27], TiO<sub>2</sub> [28–37], and Si<sub>3</sub>N<sub>4</sub> [38,39].

Static structured color has great potential for applications in the full-color display, Meta-OLED, etc. [40]. However, it is usually difficult to alter the color scheme of a structure once it has been built. As a result, the question of how to control structural color dynamically is rising in importance. The use of phase-change materials, voltage-controlled coupling, and thermal stimulation to tune the metasurface are just a few examples of the methods that have been employed to achieve the dynamic tuning of structural color. Another method that promises to be faster to tune and at the same time allow the multiplexing of structures is the combination of anisotropic structures and polarized light [41]. Brilliant structural colors under a cross-polarization condition can be achieved by the anisotropic structure's high polarization conversion [5,7,8,14,33,37,42]. Dynamically tuned electromagnetic metasurfaces using different materials properties can enable applications, such as information processing, anti-counterfeiting, and information encryption [43–48]. Inspired by the dynamic modulation of electromagnetic metasurfaces, the dynamic adjustment of structural color in the visible range by a chiral metasurface is feasible because of the synergistic effects of the chiral metasurface and polarized light [49–51].

In this work, we propose an all-dielectric chiral metasurface consisting of half-gammadion-shaped resonators embedded in PMMA and a top TiO<sub>2</sub> layer on quartz coated with an indium tin oxide (ITO) layer to realize the full-color gamut of the structural colors and anti-counterfeit functions. TiO<sub>2</sub> was selected as the material for the embedded chiral half-gammadion-shaped resonators in our design due to its near-transparency in the visible spectrum and moderate refractive index (2.4–2.7). We show a full-color gamut of the structural colors that extends well beyond sRGB by properly tuning the duty cycle ( $f_L$ ) and period ( $P$ ). The resonance peaks of the cross-polarization reflectance spectra depend on the period, thus being noticeable in color. Color mode and gray mode can be switched under the different polarization conditions. The anti-counterfeiting function is experimentally implemented by concealing the letter “A” and the Chinese word “李龙杰” inside a star pattern.

## 2. Results and Discussions

The proposed embedded chiral metasurface is schematically depicted in Figure 1a, which unfolds each layer by section. It is a square lattice of TiO<sub>2</sub> chiral half-gammadion-shaped resonators embedded in PMMA and a top TiO<sub>2</sub> layer on quartz coated with an ITO layer. The spatial inversion symmetry in the two-dimensional plane is broken by the asymmetrically protruding arms of the chiral half-gammadion-shaped resonators on the left and right sides of the central rectangular bar. The square lattice has period  $P$ ; the length and width of the chiral half-gammadion-shaped resonators are, respectively,  $L$  and  $W$ ; the thickness of the top layer TiO<sub>2</sub> layer is  $H1$ ; the height of the embedded TiO<sub>2</sub> chiral half-gammadion-shaped resonators and PMMA is  $H2$ ; and the thickness of the ITO layer is  $H3$ , as shown in Figure 1b,c. We introduce two new factors:  $f_W$  and  $f_L$ , defined as the ratios of  $W$  over the  $L/2$ , and  $L$  over the  $P$ , respectively, to simplify the design and description. Unless otherwise stated,  $f_W$ ,  $H1$ ,  $H2$ , and  $H3$  are, respectively, 0.6, 40 nm, 100 nm, and 50 nm. The embedded chiral metasurface was fabricated using a standard electron-beam lithography (EBL) and atomic layer deposition (ALD) technique followed by a selectable inductively coupled plasma (ICP)-etching process. To begin, the quartz substrate was cleaned in the ultrasound bath with acetone and absolute ethyl alcohol for 10 min, respectively, then rinsed well with deionized water. Then, a 50 nm thick ITO was deposited on the substrate with a magnetron sputtering process, improving the efficiency and saturation and facilitating the scanning electron microscope (SEM) inspection (see Figure S1). Following this step, a PMMA film was spin-coated onto the substrate and baked at 180 °C for 2 min, and the pattern layout was transferred to the PMMA resist by EBL. Next, TiO<sub>2</sub> was filled

by the conformal ALD process, where the total required film thickness is larger than the half of the maximum width of the nanostructures. At last, the top TiO<sub>2</sub> layer with different thicknesses was etched by the ICP process. Our proposed embedded chiral metasurface is beneficial for the preservation and the long-term use of the metasurface. Figure 1d presents the scanning electron microscope (SEM) images of the typical arrays of the TiO<sub>2</sub> chiral half-gammadion-shaped resonators with the ratio  $f_L$  of 0.7 and periods of 220, 300, and 380 nm. It looks a little blurry because the PMMA and top TiO<sub>2</sub> layer are not conducive. The chiral metasurface is well-fabricated except for the slightly rounded corners.

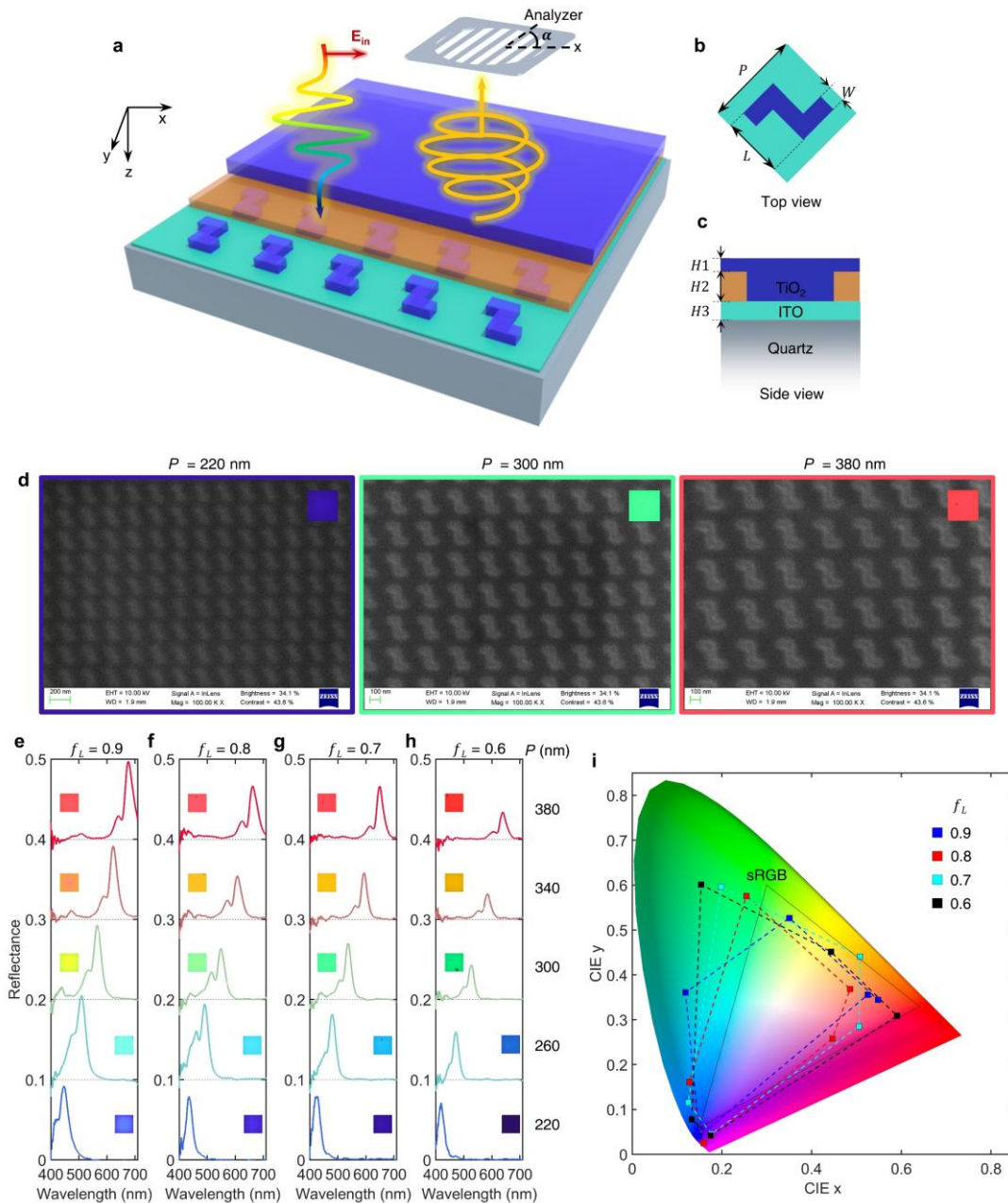


**Figure 1.** Full-color gamut of color-rendering performance of the embedded chiral metasurfaces. (a) Perspective view of the embedded chiral metasurface. (b) Top view and (c) side view of a single unit cell of the embedded chiral metasurface. (d) The top view SEM images of the embedded chiral metasurfaces with  $P$  of 220 nm, 300 nm, and 380 nm. The cross-polarization reflectance spectra and corresponding micrographs with  $f_L$  of (e) 0.9, (f) 0.8, (g) 0.7, and (h) 0.6 at different  $p$  from 220 nm to 380 nm. (i) The corresponding CIE 1931 chromaticity diagram of (e–h).

Figure 1e–h show the full-gamut color performance of the chiral metasurface with  $f_L$  from 0.9 to 0.6 and  $p$  from 220 nm to 380 nm at 40 nm intervals. The micrographs show that we successfully created full-color swatches in blue, cyan, yellow, green, orange, and red. The cross-polarization reflectance spectra are measured by a microscope and a fiber-coupled spectrometer. Here, the measured height of the top TiO<sub>2</sub> layer, PMMA layer, and ITO layer by ellipsometer are, respectively, about 40 nm, 100 nm, and 50 nm. The electric field polarization of the normally incident light is along the  $x$ -axis ( $E_{in}$ , red arrow in the oblique view schematic in Figure 1a), and there is a 45° angle between  $E_{in}$  and the arm of the half-gammadion-shaped resonator. In addition, an analyzer on the reflection direction has an angle  $\alpha$  of 90° relative to the  $x$ -axis, and the reflectance spectra  $E_{out}$  along the analyzer direction are recorded. Figure 1e–h present that the resonance peak of the measured cross-polarization reflectance spectrum is significantly red-shifted with increasing periods for each fixed  $f_L$ , indicating the color hue mainly depending on the period. All resonance peaks have an accompanying small resonance peak to the left of the main resonance peak. For each fixed period, the resonance peak is slightly blue-shifted with  $f_L$  decreasing, and the reflection efficiency decreases. Figure 1i shows the calculated chromaticity coordinates by the reflectance spectra in Figure 1e–h, which cover the full-color gamut beyond the sRGB range. The blue, red, cyan, and black square markers are, respectively, for the nanostructures with an  $f_L$  of 0.9, 0.8, 0.7, and 0.6.

We also numerically calculate the cross-polarization reflectance spectra of the chiral metasurface and the electromagnetic field at the resonant wavelength. The simulation is performed by the finite-difference time-domain (FDTD) solver, EastWave. The simulation domain is a 3D unit cell consisting of a TiO<sub>2</sub> chiral half-gammadion-shaped resonator embedded in PMMA and a top TiO<sub>2</sub> layer on quartz coated with an ITO layer. The periodic boundary conditions are applied to the  $x$ - and  $y$ -directions and the PML boundary conditions are applied to the  $z$ -dimension to absorb the outgoing waves. Quartz's refractive index was acquired from the software, PMMA's was set to 1.5, and the refractive indices of the ITO and TiO<sub>2</sub> were measured by an ellipsometer (see details about optical constants of ITO and TiO<sub>2</sub> in Figure S2 of Figure S1 Materials). The incident light is along the  $x$ -axis, and the normalized cross-polarization reflectance power was calculated by the integration of the Poynting vector at the  $y$ -direction:  $R_{cross} = \frac{1}{2} \int abs(\vec{P}_y) \cdot ds / P_s$ , where  $P_s$  is the source power. Figure 2a–d show the simulated cross-polarization reflectance spectra with an  $f_L$  from 0.9 to 0.6 and  $p$  from 220 nm to 380 nm. All the simulated cross-polarization reflectance spectra show prominent sharp resonance peaks in the visible range and have very minimal background noise, which is essential for obtaining extremely saturated colors. More importantly, the resonance peak significantly redshifts with the period increasing and the reflectance efficiency decreases with the  $f_L$  decreasing. These are consistent with the experimental results, and the comparison of the simulated and measured results are detailed in Figure S3 in Supplementary Materials. The disparity in the simulation and measurement spectra is mainly from the difference in the source incident angle. Unlike the light source conditions of vertical incidence during the simulation, in the actual measurement, the light source is of a certain aperture angle, which leads to the broadening of the resonance peak, and at the same time, the absorption introduced by the fabrication will broaden the resonant peak. The calculated cross-polarization reflectance spectra are converted to chromaticity coordinates in the CIE 1931 chromaticity diagram in Figure 2e, which demonstrates that the colors can cover the full-color gamut far beyond that of sRGB. The blue, red, cyan, and black square markers are, respectively, for the nanostructures with an  $f_L$  of 0.9, 0.8, 0.7, and 0.6. The formation of resonance peaks is the hybridized mode from the embedded nanoresonator and the array effect [19], and we calculated the field distribution of the resonance peak at the red dot marker in Figure 2b, as shown in Figure 2f. The chiral metasurface is proposed due to its excellent polarization conversion properties, which makes it have good spectral properties under cross-polarization conditions to achieve high-saturation structural colors, and at the same time, our proposed

embedded metasurface is less susceptible to damage and has the advantage that it can be used for a long time compared to other structural color work.

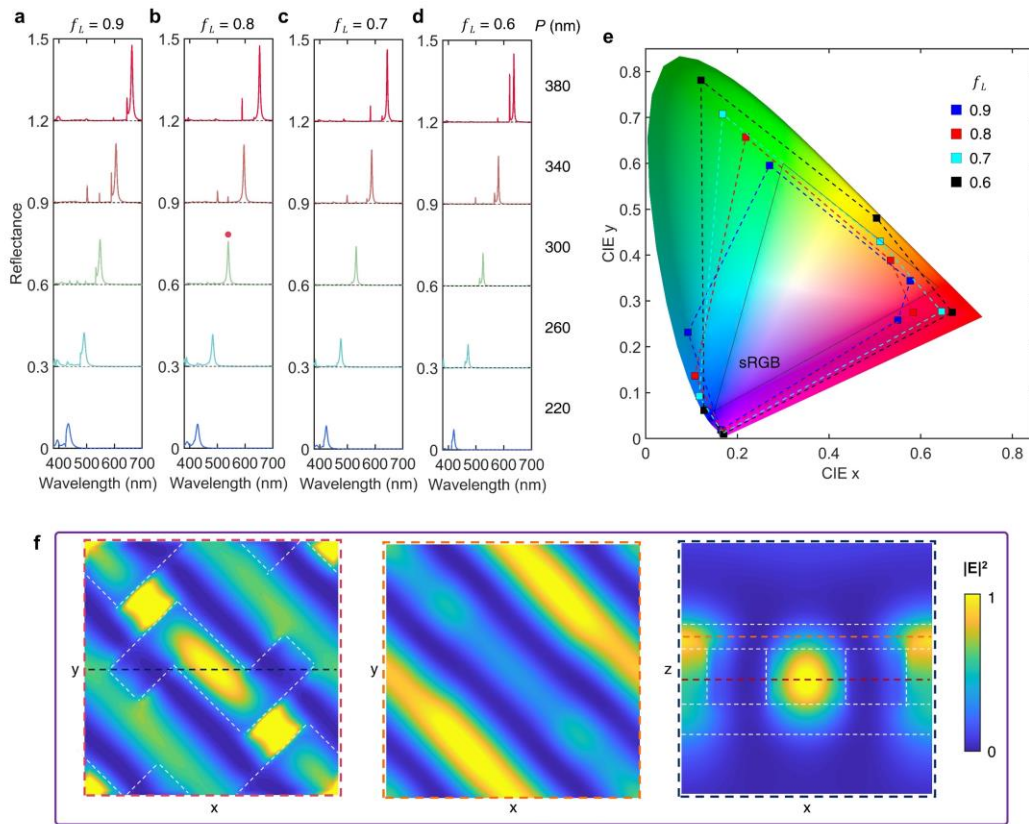


**Figure 2.** The color performance of simulated embedded chiral metasurface with different  $f_L$  and  $P$ . The cross-polarization reflectance spectra and corresponding micrographs with  $f_L$  of (a) 0.9, (b) 0.8, (c) 0.7, and (d) 0.6 at different  $p$  from 220 nm to 380 nm. (e) The corresponding CIE 1931 chromaticity diagram of (a–d). (f) The square of the absolute of the electric field distributions  $|E|^2$  at the  $xy$ - and  $xz$ -plane of resonant peaks in (b) marked by a magenta dot.

The proposed embedded chiral metasurfaces have different modes under different observation conditions, such as those illustrated in Figure 3a,b. Figure 3a has a vibrant structural color covering the full-color gamut in Figure 3c under cross-polarization conditions with different periods from 220 nm to 400 nm, which we call the color mode. As a comparison, we observe the corresponding structural color at the angle of 135 degrees between the polarizer and the analyzer, which loses its bright color covering the full gamut. The change in the above conditions (the period and rotation angle of a single structure) does not change the hue but presents a grayish-yellow color, which we call the gray mode. The corresponding chromaticity diagram in Figure 3c also shows that its gamut changes very little and all the chromaticity coordinates are close to the white point, which is difficult to recognize with our naked eye. This feature allows us to use it to switch between the color and gray modes. The fabricated “rainbow” shows bright colors under cross-polarization conditions, as in Figure 3d, and dull colors in gray mode, as in Figure 3e. The stitching traces in Figure 3e are caused by two photographs due to the large area of “rainbow”.

The proposed embedded chiral metasurface is anti-counterfeit due to its different color performance under different observation conditions (e.g., no polarization, single-polarization, and cross-polarization). As a proof of concept, we have designed and fabricated cryptographic nanoprints of a star encrypted with the letter “A” and the Chinese word “李龙杰” which can only be decoded in the designated cross-polarization. The period parameters of the star, the Chinese word “李龙杰”, and the letter “A” are, respectively, 540 nm, 580 nm, and 620 nm. The other parameters  $f_L$ ,  $f_W$ ,  $H1$ ,  $H2$ , and  $H3$  are, respec-

tively, 0.7, 0.6, 110 nm, 100 nm, and 50 nm. In the absence of polarization, which is the observation condition in our daily life, we can only observe a pink star, in which we can barely observe the Chinese word “李龙杰” and letter “A” with the naked eye, as shown in Figure 4a. When the polarization direction is 0 or 90 degrees from the horizontal direction of the star, we can only see the internal information dimly, as shown in Figure 4b. When we observe using cross-polarization, the information will be decoded and we can visibly observe it with the naked eye, as shown in Figure 4c. The star changes colors and the embedded information becomes more or less clear as we rotate the sample. The letter “A” is easier to make out at any rotation angle, while the Chinese word “李龙杰” is less distinct at 0 and 72 degrees, while it is very clear at 36, 108, and 144 degrees. In the case of cross-polarization, where the incident polarization and the reflected polarization are perpendicular to one another, only a few specific incident and reflected polarization tools are capable of fully decoding the encrypted information recorded in the embedded chiral metasurface. These phenomena offer platforms for use in cryptography and other secure applications. Figure 4d presents the SEM images of the full view of the entire star and one of the corners, where each pixel is made of the proposed embedded chiral metasurface.

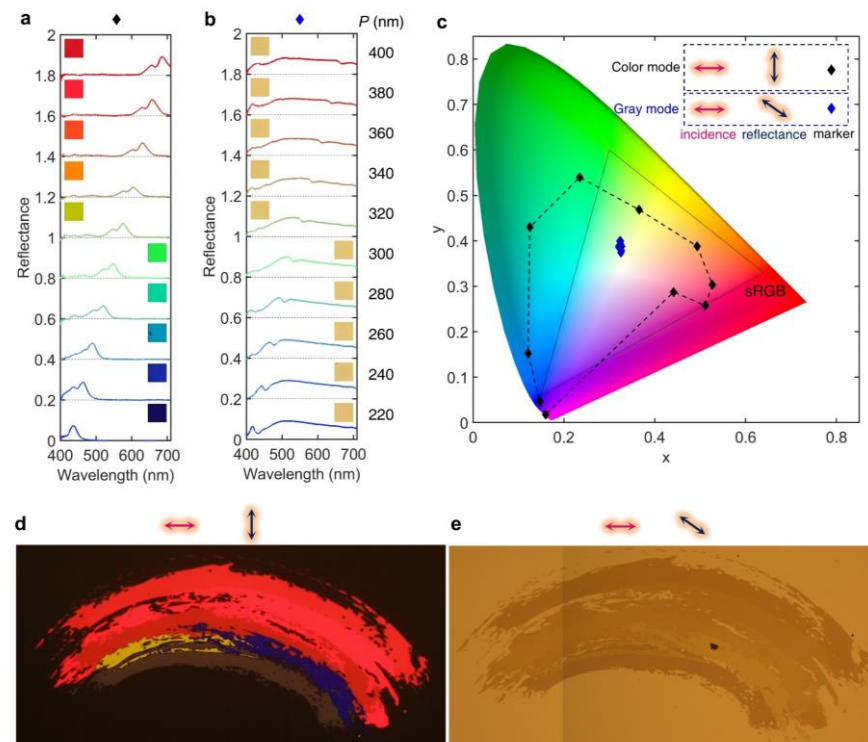


**Figure 3.** The color performance of fabricated embedded chiral metasurface under different observation conditions. (a) Reflectance spectra and micrographs of the embedded chiral metasurface under cross-polarization observation conditions (0 degree incidence, 90 degree reflectance). (b) Reflectance spectra and micrographs of the embedded chiral metasurface under observation conditions of 0 degree incidence and 135 degree reflectance. (c) The corresponding CIE 1931 chromaticity diagram of (a,b). Rainbow images in (d) color mode and (e) gray mode.

As an auxiliary validation, we calculated the reflectance spectra of the structures with periods of 540 nm, 580 nm, and 620 nm under different polarization light conditions, as shown in Figure 5a–c. The parameters of this design are the same as those of the previous section, with the exception that  $f_L$  and  $H1$  are 0.7 and 110 nm, respectively. The polarization conditions for the three reflectance spectra are the polarized light parallel to the x-axis, calculating the single-polarized reflectance spectrum, as shown in Figure 5a; the polarized light perpendicular to x-axis, calculating the single-polarized reflectance spectrum, as shown in Figure 5b; and the polarized parallel to light x-axis, calculating the cross-

polarized reflectance spectrum, as shown in Figure 5c. The cross-polarized reflectance spectra become more noticeable than that of the first two single-polarization shifts when the period is changed from 540 nm to 620 nm. In the 1931 CIE chromaticity diagram, it is obvious that, with the period increasing, the color from the cross-polarization reflectance changes (the blue square dot), while the colors from the single-polarized reflectance spectrum hardly change (red and cyan dots), as shown in Figure 5d. The anti-counterfeiting function is aided by such a spectral performance.

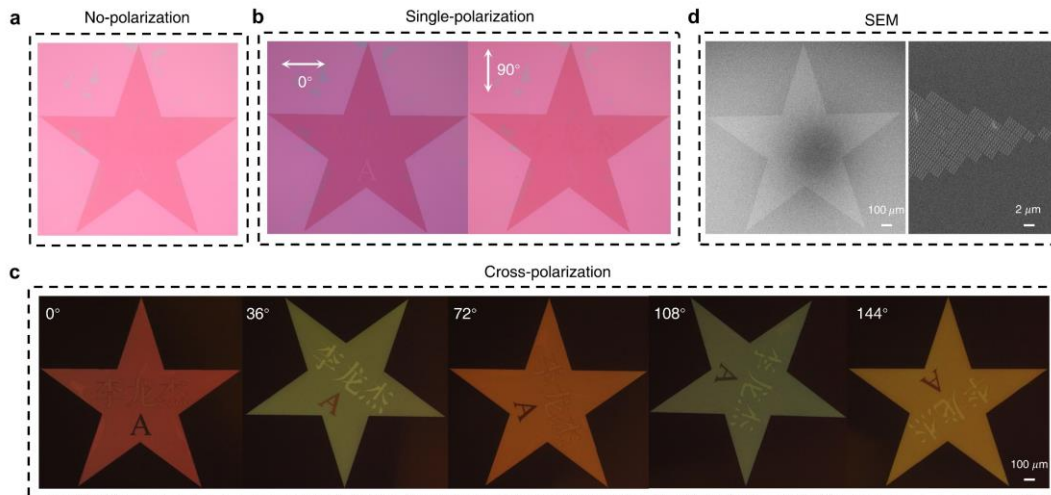


**Figure 4.** Anti-counterfeiting feature of the embedded chiral metasurfaces. (a) Micrograph of a star with encrypted information under no polarization. (b) Micrograph of a star with encrypted information under single-polarization (0 degrees or 90 degrees). (c) Micrograph of a star with encrypted information under cross-polarization with the sample rotated at an angle of 0, 36, 72, 108, and 144 degrees. (d) The top view SEM images of the entire star and one of the corners consist of embedded chiral metasurfaces.

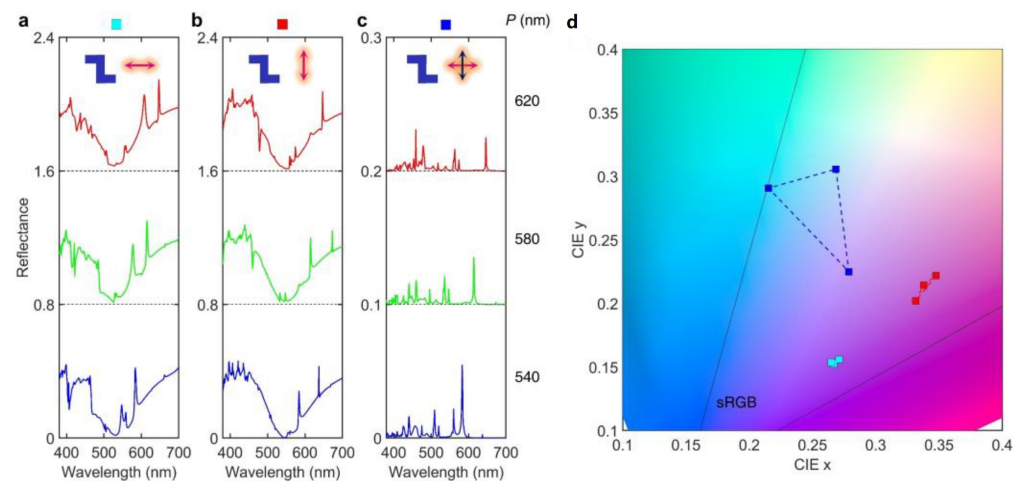


**Figure 5.** The color performance of embedded chiral metasurface with different  $P$  from 540 nm to 620 nm. The reflectance spectra under (a) single-polarization with 0 degrees to the x-axis, (b) single-polarization with 90 degrees with 90 degrees to the x-axis, (c) cross-polarization at different  $p$  from 540 nm to 620 nm. (d) The corresponding CIE 1931 chromaticity diagram of (a–c).

### 3. Conclusions

In summary, we have demonstrated the full-color gamut of the structural colors and anti-counterfeit functions of an all-dielectric chiral metasurface consisting of half-gammadion-shaped resonators embedded in PMMA and a top  $TiO_2$  layer on quartz coated

with an ITO layer. The excellent polarization conversion characteristics of the chiral structure are exploited, while the embedded structure is less susceptible to damage and thus better protected for the long-term use of the metasurface. Cross-polarization resonance peaks cross the visible range with the period  $p$  (from 220 nm to 380 nm) and  $f_L$  (from 0.6 to 0.9), resulting in highly saturated structured colors covering the full-color gamut considerably beyond sRGB. Moreover, we experimentally verify that the proposed embedded chiral metasurface can switch modes under different observation conditions: color mode and gray mode. Further, we designed and fabricated a star with internal hidden information including the letter “A” and the Chinese word “李龙杰”, achieving complete information decoding under cross-polarization, which is thus the anti-counterfeiting effect. This research has significant implications in micro-display, nano-printing, anti-counterfeiting, and information encryption.

**Supplementary Materials:** The following supporting information can be downloaded at: <https://www.mdpi.com/article/10.3390/photonics10040401/s1>, Figure S1: Comparison of reflectance with and without ITO layer; Figure S2: Optical constants of ITO and TiO<sub>2</sub>; Figure S3: Comparison of simulated and measured cross-polarization reflectance spectra.

**Author Contributions:** Conceptualization, L.S.; methodology, L.L. and L.S.; software, L.L., H.L., X.S. and J.H.; validation, L.L., H.H., H.X., C.L., S.Z. and J.N. investigation, L.L.; resources, L.S.; writing—original draft preparation, L.L., L.S. and J.N.; writing—review and editing, L.L., L.S. and J.N.; visualization, L.L. and H.L.; funding acquisition, L.S. All authors have read and agreed to the published version of the manuscript.

**Funding:** The research was funded by the National Natural Science Foundation of China (Grant Nos. 61875225, 61888102).

**Data Availability Statement:** Not applicable.

**Conflicts of Interest:** The authors declare no conflict of interest.

## References

1. Dean, N. Colouring at the nanoscale. *Nat. Nanotechnol.* **2015**, *10*, 15–16. [[CrossRef](#)] [[PubMed](#)]
2. Baranov, D.G.; Zuev, D.A.; Lepeshov, S.I.; Kotov, O.V.; Krasnok, A.E.; Evlyukhin, A.B.; Chichkov, B.N. All-dielectric nanophotonics: The quest for better materials and fabrication techniques. *Optica* **2017**, *4*, 814. [[CrossRef](#)]
3. Kumar, K.; Duan, H.; Hegde, R.S.; Koh, S.C.W.; Wei, J.N.; Yang, J.K.W. Printing colour at the optical diffraction limit. *Nat. Nanotechnol.* **2012**, *7*, 557–561. [[CrossRef](#)] [[PubMed](#)]
4. Lu, B.-R.; Xu, C.; Liao, J.; Liu, J.; Chen, Y. High-resolution plasmonic structural colors from nanohole arrays with bottom metal disks. *Opt. Lett.* **2016**, *41*, 1400. [[CrossRef](#)]
5. Wang, X.; Xu, D.; Jaquet, B.; Yang, Y.; Wang, J.; Huang, H.; Chen, Y.; Gerhard, C.; Zhang, K. Structural Colors by Synergistic Birefringence and Surface Plasmon Resonance. *ACS Nano* **2020**, *14*, 16832–16839. [[CrossRef](#)]
6. Shaltout, A.M.; Kim, J.; Boltasseva, A.; Shalaev, V.M.; Kildishev, A.V. Ultrathin and multicolour optical cavities with embedded metasurfaces. *Nat. Commun.* **2018**, *9*, 2673. [[CrossRef](#)]
7. Jiang, M.; Siew, S.Y.; Chan, J.Y.E.; Deng, J.; Wu, Q.Y.S.; Jin, L.; Yang, J.K.W.; Teng, J.; Danner, A.; Qiu, C.-W. Patterned resist on flat silver achieving saturated plasmonic colors with sub-20-nm spectral linewidth. *Mater. Today* **2020**, *35*, 99–105. [[CrossRef](#)]
8. Kim, Y.; Jung, K.; Cho, J.; Hyun, J.K. Realizing Vibrant and High-Contrast Reflective Structural Colors from Lossy Metals Supporting Dielectric Gratings. *ACS Nano* **2019**, *13*, 10717–10726. [[CrossRef](#)]
9. Jung, Y.; Jung, H.; Choi, H.; Lee, H. Polarization Selective Color Filter Based on Plasmonic Nanograting Embedded Etalon Structures. *Nano Lett.* **2020**, *20*, 6344–6350. [[CrossRef](#)]
10. Hail, C.U.; Schnoering, G.; Damak, M.; Poulidakos, D.; Eghlidi, H. A Plasmonic Painter’s Method of Color Mixing for a Continuous Red–Green–Blue Palette. *ACS Nano* **2020**, *14*, 1783–1791. [[CrossRef](#)]
11. Shrestha, V.R.; Lee, S.-S.; Kim, E.-S.; Choi, D.-Y. Aluminum Plasmonics Based Highly Transmissive Polarization-Independent Subtractive Color Filters Exploiting a Nanopatch Array. *Nano Lett.* **2014**, *14*, 6672–6678. [[CrossRef](#)]
12. Tan, S.J.; Zhang, L.; Zhu, D.; Goh, X.M.; Wang, Y.M.; Kumar, K.; Qiu, C.-W.; Yang, J.K.W. Plasmonic Color Palettes for Photorealistic Printing with Aluminum Nanostructures. *Nano Lett.* **2014**, *14*, 4023–4029. [[CrossRef](#)]
13. Zhu, X.; Vannahme, C.; Højlund-Nielsen, E.; Mortensen, N.A.; Kristensen, A. Plasmonic colour laser printing. *Nat. Nanotechnol.* **2016**, *11*, 325–329. [[CrossRef](#)]
14. Song, M.; Wang, D.; Kudyshev, Z.A.; Xuan, Y.; Wang, Z.; Boltasseva, A.; Shalaev, V.M.; Kildishev, A.V. Enabling Optical Steganography, Data Storage, and Encryption with Plasmonic Colors. *Laser Photonics Rev.* **2021**, *15*, 2000343. [[CrossRef](#)]

15. Shi, L.; Niu, J.; Li, L.; Wang, C.; Shang, X.; Zhang, P.; Liu, Y.; Zhang, Y. Deep Subwavelength Wide-Angle Structural Colors at the Single Pixel Level. *Adv. Opt. Mater.* **2022**, *10*, 2200552. [[CrossRef](#)]
16. Yang, B.; Cheng, H.; Chen, S.; Tian, J. Structural colors in metasurfaces: Principle, design and applications. *Mater. Chem. Front.* **2019**, *3*, 750–761. [[CrossRef](#)]
17. Liu, X.; Huang, Z.; Zang, J. All-Dielectric Silicon Nanoring Metasurface for Full-Color Printing. *Nano Lett.* **2020**, *20*, 8739–8744. [[CrossRef](#)]
18. Yang, W.; Xiao, S.; Song, Q.; Liu, Y.; Wu, Y.; Wang, S.; Yu, J.; Han, J.; Tsai, D.-P. All-dielectric metasurface for high-performance structural color. *Nat. Commun.* **2020**, *11*, 1864. [[CrossRef](#)]
19. Jang, J.; Badloe, T.; Yang, Y.; Lee, T.; Mun, J.; Rho, J. Spectral Modulation through the Hybridization of Mie-Scatterers and Quasi-Guided Mode Resonances: Realizing Full and Gradients of Structural Color. *ACS Nano* **2020**, *14*, 15317–15326. [[CrossRef](#)]
20. Xu, Z.; Xu, Z.; Li, N.; Dong, Y.; Fu, Y.H.; Hu, T.; Zhong, Q.; Zhou, Y.; Li, D.; Zhu, S.; et al. Metasurface-based subtractive color filter fabricated on a 12-inch glass wafer using a CMOS platform. *Photon. Res. PRJ* **2021**, *9*, 13–20. [[CrossRef](#)]
21. Li, L.; Niu, J.; Shang, X.; Chen, S.; Lu, C.; Zhang, Y.; Shi, L. Bright Field Structural Colors in Silicon-on-Insulator Nanostructures. *ACS Appl. Mater. Interfaces* **2021**, *13*, 4364–4373. [[CrossRef](#)] [[PubMed](#)]
22. Liang, C.; Liang, C.; Deng, L.; Deng, L.; Dai, Q.; Li, Z.; Zheng, G.; Zheng, G.; Zheng, G.; et al. Single-celled multifunctional metasurfaces merging structural-color nanoprinting and holography. *Opt. Express* **2021**, *29*, 10737–10748. [[CrossRef](#)] [[PubMed](#)]
23. Lee, T.; Kim, J.; Koirala, I.; Yang, Y.; Badloe, T.; Jang, J.; Rho, J. Nearly Perfect Transmissive Subtractive Coloration through the Spectral Amplification of Mie Scattering and Lattice Resonance. *ACS Appl. Mater. Interfaces* **2021**, *13*, 26299–26307. [[CrossRef](#)] [[PubMed](#)]
24. Dong, Z.; Jin, L.; Rezaei, S.D.; Wang, H.; Chen, Y.; Tjiptoharsono, F.; Ho, J.; Gorelik, S.; Ng, R.J.H.; Ruan, Q.; et al. Schrödinger's red pixel by quasi-bound-states-in-the-continuum. *Sci. Adv.* **2022**, *8*, eabm4512. [[CrossRef](#)]
25. Badloe, T.; Kim, J.; Kim, I.; Kim, W.-S.; Kim, W.S.; Kim, Y.-K.; Rho, J. Liquid crystal-powered Mie resonators for electrically tunable photorealistic color gradients and dark blacks. *Light Sci. Appl.* **2022**, *11*, 118. [[CrossRef](#)]
26. Shang, X.; Niu, J.; Wang, C.; Li, L.; Lu, C.; Zhang, Y.; Shi, L. Mie Resonances Enabled Subtractive Structural Colors with Low-Index-Contrast Silicon Metasurfaces. *ACS Appl. Mater. Interfaces* **2022**, *14*, 55933–55943. [[CrossRef](#)]
27. Hentschel, M.; Koshelev, K.; Sterl, F.; Both, S.; Karst, J.; Shamsafar, L.; Weiss, T.; Kivshar, Y.; Giessen, H. Dielectric Mie voids: Confining light in air. *Light Sci. Appl.* **2023**, *12*, 3. [[CrossRef](#)]
28. Sun, S.; Zhou, Z.; Zhang, C.; Gao, Y.; Duan, Z.; Xiao, S.; Song, Q. All-Dielectric Full-Color Printing with TiO<sub>2</sub> Metasurfaces. *ACS Nano* **2017**, *11*, 4445–4452. [[CrossRef](#)]
29. Sun, S.; Yang, W.; Zhang, C.; Jing, J.; Gao, Y.; Yu, X.; Song, Q.; Xiao, S. Real-Time Tunable Colors from Microfluidic Reconfigurable All-Dielectric Metasurfaces. *ACS Nano* **2018**, *12*, 2151–2159. [[CrossRef](#)]
30. Koirala, I.; Lee, S.-S.; Choi, D.-Y. Highly transmissive subtractive color filters based on an all-dielectric metasurface incorporating TiO<sub>2</sub> nanopillars. *Opt. Express* **2018**, *26*, 18320. [[CrossRef](#)]
31. Yang, B.; Liu, W.; Li, Z.; Cheng, H.; Choi, D.-Y.; Chen, S.; Tian, J. Ultrahighly Saturated Structural Colors Enhanced by Multipolar-Modulated Metasurfaces. *Nano Lett.* **2019**, *19*, 4221–4228. [[CrossRef](#)]
32. Zhang, C.; Jing, J.; Wu, Y.; Fan, Y.; Yang, W.; Wang, S.; Song, Q.; Xiao, S. Stretchable All-Dielectric Metasurfaces with Polarization-Insensitive and Full-Spectrum Response. *ACS Nano* **2020**, *14*, 1418–1426. [[CrossRef](#)]
33. Huo, P.; Huo, P.; Song, M.; Song, M.; Zhu, W.; Zhu, W.; Zhang, C.; Chen, L.; Chen, L.; Lezec, H.J.; et al. Photorealistic full-color nanopainting enabled by a low-loss metasurface. *Optica* **2020**, *7*, 1171–1172. [[CrossRef](#)]
34. Eaves-Rathert, J.; Kovalik, E.; Ugwu, C.F.; Rogers, B.R.; Pint, C.L.; Valentine, J.G. Dynamic Color Tuning with Electrochemically Actuated TiO<sub>2</sub> Metasurfaces. *Nano Lett.* **2022**, *22*, 1626–1632. [[CrossRef](#)]
35. Li, H.; Li, H.; Xu, Y.; Zhang, X.; Xiao, X.; Zhou, F.; Zhang, Z. All-dielectric high saturation structural colors enhanced by multipolar modulated metasurfaces. *Opt. Express* **2022**, *30*, 28954–28965. [[CrossRef](#)]
36. Yang, B.; Ma, D.; Liu, W.; Choi, D.-Y.; Li, Z.; Cheng, H.; Cheng, H.; Tian, J.; Chen, S.; Chen, S.; et al. Deep-learning-based colorimetric polarization-angle detection with metasurfaces. *Optica* **2022**, *9*, 217–220. [[CrossRef](#)]
37. Li, L.; Niu, J.; Wang, C.; Shang, X.; Xue, H.; Hu, J.; Li, H.; Lu, C.; Zhao, S.; Zhang, Y.; et al. High-Saturation Full-Color Printing with All-Dielectric Chiral Metasurfaces. *ACS Appl. Mater. Interfaces* **2023**.
38. Park, C.-S.; Koirala, I.; Gao, S.; Shrestha, V.R.; Lee, S.-S.; Choi, D.-Y. Structural color filters based on an all-dielectric metasurface exploiting silicon-rich silicon nitride nanodisks. *Opt. Express* **2019**, *27*, 667. [[CrossRef](#)]
39. Yang, J.-H.; Babicheva, V.E.; Yu, M.-W.; Lu, T.-C.; Lin, T.-R.; Chen, K.-P. Structural Colors Enabled by Lattice Resonance on Silicon Nitride Metasurfaces. *ACS Nano* **2020**, *14*, 5678–5685. [[CrossRef](#)]
40. Daqiqeh Rezaei, S.; Dong, Z.; You En Chan, J.; Trisno, J.; Ng, R.J.H.; Ruan, Q.; Qiu, C.-W.; Mortensen, N.A.; Yang, J.K.W. Nanophotonic Structural Colors. *ACS Photonics* **2021**, *8*, 18–33. [[CrossRef](#)]
41. Ko, J.H.; Yoo, Y.J.; Lee, Y.; Jeong, H.-H.; Song, Y.M. A review of tunable photonics: Optically active materials and applications from visible to terahertz. *iScience* **2022**, *25*, 104727. [[CrossRef](#)] [[PubMed](#)]
42. Kim, I.; Jang, J.; Kim, G.; Lee, J.; Badloe, T.; Mun, J.; Rho, J. Pixelated bifunctional metasurface-driven dynamic vectorial holographic color prints for photonic security platform. *Nat. Commun.* **2021**, *12*, 3614. [[CrossRef](#)] [[PubMed](#)]

43. Chen, L.; Ma, Q.; Luo, S.S.; Ye, F.J.; Cui, H.Y.; Cui, T.J. Touch-Programmable Metasurface for Various Electromagnetic Manipulations and Encryptions. *Small* **2022**, *18*, 2203871. [[CrossRef](#)] [[PubMed](#)]
44. Wang, H.; Qin, Z.; Huang, L.; Li, Y.; Zhao, R.; Zhou, H.; He, H.; Zhang, J.; Qu, S. Metasurface with dynamic chiral meta-atoms for spin multiplexing hologram and low observable reflection. *Photonix* **2022**, *3*, 10. [[CrossRef](#)]
45. Ma, Q.; Gao, W.; Xiao, Q.; Ding, L.; Gao, T.; Zhou, Y.; Gao, X.; Yan, T.; Liu, C.; Gu, Z.; et al. Directly wireless communication of human minds via non-invasive brain-computer-metasurface platform. *eLight* **2022**, *2*, 11. [[CrossRef](#)]
46. Mehmood, M.Q.; Seong, J.; Naveed, M.A.; Kim, J.; Zubair, M.; Riaz, K.; Massoud, Y.; Rho, J. Single-Cell-Driven Tri-Channel Encryption Meta-Displays. *Adv. Sci.* **2022**, *9*, 2203962. [[CrossRef](#)]
47. Bao, Y.; Yu, Y.; Xu, H.; Guo, C.; Li, J.; Sun, S.; Zhou, Z.-K.; Qiu, C.-W.; Wang, X.-H. Full-colour nanoprint-hologram synchronous metasurface with arbitrary hue-saturation-brightness control. *Light Sci. Appl.* **2019**, *8*, 95. [[CrossRef](#)]
48. Javed Satti, A.; Ashar Naveed, M.; Javed, I.; Mahmood, N.; Zubair, M.; Qasim Mehmood, M.; Massoud, Y. A highly efficient broadband multi-functional metaplate. *Nanoscale Adv.* **2023**, *5*, 2010–2016. [[CrossRef](#)]
49. Zhang, Y.; Shi, L.; Zhang, R.-Y.; Duan, J.; Ng, J.; Chan, C.T.; Fung, K.H. Metric-Torsion Duality of Optically Chiral Structures. *Phys. Rev. Lett.* **2019**, *122*, 200201. [[CrossRef](#)]
50. Choi, S.; Son, H.; Lee, B. Chirality-selective all-dielectric metasurface structural color display. *Opt. Express* **2021**, *29*, 41258–41267. [[CrossRef](#)]
51. Shu, X.; Li, A.; Hu, G.; Wang, J.; Alù, A.; Chen, L. Fast encirclement of an exceptional point for highly efficient and compact chiral mode converters. *Nat. Commun.* **2022**, *13*, 2123. [[CrossRef](#)]

**Disclaimer/Publisher's Note:** The statements, opinions and data contained in all publications are solely those of the individual author(s) and contributor(s) and not of MDPI and/or the editor(s). MDPI and/or the editor(s) disclaim responsibility for any injury to people or property resulting from any ideas, methods, instructions or products referred to in the content.